

# Theoretical Study of Cellulose II Nanocrystals with Different Exposed Facets

**Can Leng**

National University of Defense Technology

**Kenli Li**

Hunan University

**Zean Tian** (✉ [tianzean@hnu.edu.cn](mailto:tianzean@hnu.edu.cn))

Hunan University

**Yubing Si**

Zhengzhou University

**Huang Huang**

National Supercomputer Center in Changsha

**Junfeng Li**

Luoyang Normal University

**Jie Liu**

National University of Defense Technology

**Wei-Qing Huang**

Hunan University

**Keqin Li**

Hunan University

---

## Research Article

**Keywords:** physicochemical properties, hydrogen bond, natural polymer

**Posted Date:** February 17th, 2021

**DOI:** <https://doi.org/10.21203/rs.3.rs-228153/v1>

**License:** © ⓘ This work is licensed under a Creative Commons Attribution 4.0 International License.

[Read Full License](#)

---

# Theoretical Study of Cellulose II Nanocrystals with Different Exposed Facets

Can Leng<sup>1,2,3</sup>, Kenli Li<sup>3,4</sup>, Zean Tian<sup>4\*</sup>, Yubing Si<sup>5\*\*</sup>, Huang Huang<sup>3</sup>, Junfeng Li<sup>6</sup>, Jie Liu<sup>1,2</sup>, Wei-Qing Huang<sup>7</sup>, and Keqin Li<sup>4,8\*\*\*</sup>

<sup>1</sup>Science and Technology on Parallel and Distributed Processing Laboratory, National University of Defense Technology, Changsha 410073, China

<sup>2</sup>Laboratory of Software Engineering for Complex Systems, National University of Defense Technology, Changsha 410073, China

<sup>3</sup>National Supercomputer Center in Changsha, 410082, China

<sup>4</sup>College of Computer Science and Electronic Engineering, Hunan University, Changsha 410082, China

<sup>5</sup>College of Chemistry, Zhengzhou University, Zhengzhou, 450001, China

<sup>6</sup>College of Chemistry and Chemical Engineering, and Henan Key Laboratory of Function-Oriented Porous Materials, Luoyang Normal University, 471934 Luoyang, China

<sup>7</sup>Department of Applied Physics, School of Physics and Electronics, Hunan University, Changsha 410082, China

<sup>8</sup>Department of Computer Science, State University of New York, New Paltz, New York 12561, USA

\*tianzean@hnu.edu.cn

\*\*ybsi@zzu.edu.cn

\*\*\*lik@newpaltz.edu

## ABSTRACT

Derived from the most abundant natural polymer, cellulose nanocrystal materials have attracted attention in recent decades due to their chemical and mechanical properties. However, still unclear is the influence of different exposed facets of the cellulose nanocrystals on the physicochemical properties. Herein, we first design cellulose II nanocrystals with different exposed facets, the hydroxymethyl conformations distribution, hydrogen bond (HB) analysis, as well as the relative structural stability of these models (including crystal facets {A, B, O} and Type-A models vary in size) are theoretically investigated. The results reveal that the HB network of terminal anhydroglucose depends on the adjacent chain's contact sites in nanocrystals exposed with different facets. Compared to nanocrystals exposed with inclined facet, these exposed with flat facet tend to be the most stable. Therefore, the strategy of tuning exposed crystal facets will guide the design of novel cellulose nanocrystals with various physicochemical properties.

## Introduction

As an environmentally friendly and low-cost material, cellulose has been widely used in medicinal, environmental, and separation technologies in recent decades.<sup>1-3</sup> Cellulose is composed by linear chains of ringed glucose in which the highly ordered and disordered structures can form crystalline and amorphous-like, respectively. In general, there are four distinct crystalline celluloses in two groups of the natural fiber on earth (cellulose I), and the man-made fibers from synthesis (cellulose II, III, and IV).<sup>4</sup> Cellulose II that the chains polarity is antiparallel to each other<sup>5-7</sup> is derived from cellulose I<sup>8</sup> by either mercerization or regeneration processes. Among the chains opposite to each other in cellulose II, the outer one is usually assigned as Origin (O) and the inner one as Center (C), respectively.<sup>9</sup> Moreover, the hydroxymethyl group structure of cellulose II is different from cellulose I. Contrary to the trans-gauche (tg) conformation of cellulose I<sup>10,11</sup>, cellulose II adopts a gauche-trans (gt) conformation<sup>5-7</sup>, which can be diversified in gauche-gauche (gg) conformation<sup>12</sup> in some small crystal morphologies.

Cellulose nanocrystals refer to the size of cellulose crystalline on the nanoscale. The relative stability of cellulose nanocrystals varies with their crystalline forms. For example, Navarrete-López et al.<sup>13</sup> reported that cellulose I $\beta$  is more stable than cellulose I $\alpha$  due to the weak interaction between layer chain arrangement. Goldberg et al.<sup>14</sup> have studied the quantitative order of stability for cellulose through experimental methods and showed that the stability of cellulose III is higher than cellulose II, followed by cellulose I $\beta$ . On the other hand, the cellulose nanocrystals with different shapes and sizes have different relative stability due to the energy discrepancy of different facets and inter-sheet interactions (such as hydrophobic interactions and weak hydrogen bonds). For instance, it has been demonstrated that the 234432 chain arrangement based on 6 layers cellulose nanocrystals is more stable than the 34443 chain arrangement based on 5-layer with the same 18 cellulose polymer chains.<sup>15</sup> In order to explore the mechanism of the relative stability of cellulose nanocrystals, a series of theoretical study has been conducted<sup>16-18</sup> in recent years. For instance, Yui studied<sup>19</sup> the structural stability of the solvated cellulose III<sub>I</sub> crystal through molecular dynamics (MD) simulation and confirmed the metastable properties of cellulose III<sub>I</sub> by the reversible transition to the cellulose I $\beta$  due to the quarter staggered structure along the axis direction. The structural stability of the finite molecular chain cellulose I $\alpha$ , I $\beta$ , II, and III by density functional theory (DFT) by Uto et al.,<sup>20</sup> indicated that the stacking and crystal transformation of cellulose crystals were mainly affected by the different stacking methods of the cellulose backbone. A calculation<sup>21</sup> (mixed MD with DFT) was adopted to investigate the relative structural energy of native plant cellulose with different shapes to evaluate its relative stability. However, due to the computational bottleneck caused by the Kohn-Sham (KS) equation<sup>22,23</sup>, conventional DFT calculations are usually limited to a few hundred atoms. Thanks to the development of semi-empirical methods in recent years<sup>24-26</sup>, it is possible to conduct simulations for a large molecular system including thousands of atoms.

Hydrogen bond (HB) is an essential factor that influences the physicochemical properties of cellulose nanocrystals<sup>27-29</sup>. In the crystalline cellulose, three-dimensional hydrogen-bonded networks formed by hydroxyl groups, as well as a large number of covalent bonds (i.e., C-O, C-H, O-H), comprise the cellulose backbone. Particularly, these HB linkages play an important role in chain stiffness and stability of the cellulose<sup>30,31</sup>. Experiments have shown that HB networks can be regulated and resulted in different crystal morphologies<sup>10,32,33</sup>. For example, different HB networks can be formed on some anhydroglucose residues not fully confirmed, which are speculated by Idström et al.,<sup>34</sup> to be related to different exposed facets of regenerated cellulose. Therefore, different crystal morphologies can be obtained by regulating the HB network, thus, resulting in different properties. Unfortunately, these HBs structure of cellulose is difficult to be directly determined experimentally because of the inaccuracy of hydrogen atoms using classical techniques such as X-rays and neutron diffraction. Even worse, due to some cellulose's small diameter with partially disordered regions on the surface, it is currently difficult to accurately study the HB distance<sup>35</sup> and hydroxymethyl groups where each glucose residue unit rotates with respect to the ring atoms<sup>36</sup> through experimental techniques. Therefore, it is challenging to design novel cellulose nanocrystals exposed different facets, which are relatively stable by modulating HBs to obtain desirable specific properties and functions.

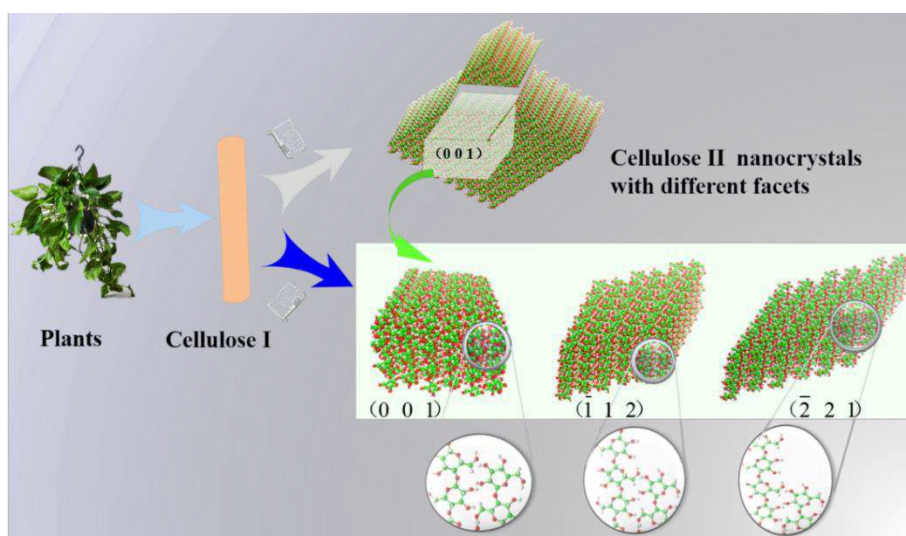


**Figure 1. Cellulose II nanocrystals with different exposed facets.** Cellulose I represent the native material in plants, from which Cellulose II can be synthesized. The facet (0 0 1) is the primary crystal facets of cellulose II nanocrystals,  $(\bar{1} \ 1 \ 2)$  and  $(\bar{2} \ 2 \ 1)$  are the inclined facets of cellulose II.

## Results and discussion

In this work, we first theoretically design several cellulose II nanocrystals that expose (0 0 1),  $(\bar{1} \ 1 \ 2)$ , and  $(\bar{2} \ 2 \ 1)$  facets respectively, by tuning the size of chains and/or HBs. The MD simulation and DFT calculations are carried out to investigate the hydroxymethyl structures, HBs properties and their relative structural stability. We find that different contact sites between the ends

of the adjacent chains can affect the HB formation of terminal anhydroglucose. The relative stability of cellulose II nanocrystals is dependent on their inclined facets. The results obtained in this work are useful to synthesize novel celluloses with different physicochemical properties.

**Table 1.** Dimensions and number of molecules for the six types of cellulose II nanocrystal models.

The label of crystals model	Base plane dimensions	No. of chains	DP	No. of water
6A6	$6(1\bar{1}0) \times 6(110) \times 6(\bar{1}12)$	36	6	12532
6A12	$6(1\bar{1}0) \times 6(110) \times 12(\bar{1}12)$	36	12	16299
6A19	$6(1\bar{1}0) \times 6(110) \times 19(\bar{1}12)$	36	19	37444
10A12	$10(1\bar{1}0) \times 10(110) \times 12(\bar{1}12)$	100	12	45148
6B12	$6(1\bar{1}0) \times 6(110) \times 12(\bar{2}21)$	36	12	20576
6O12	$6(1\bar{1}0) \times 6(110) \times 12(001)$	36	12	12171

The six cellulose II nanocrystal models are constructed based on a toolkit developed by Gomes.<sup>37</sup> The model parameters are shown in Table 1, and Fig. 1 shows the detailed structures. In these nanocrystal models, there are three types of the exposed facets with the index of  $(\bar{1}12)$ ,  $(\bar{2}21)$ , and  $(001)$ , labeled as A, B, and O in the paper for convenience. The facets A and B are derived from O that is the usual crystal facet  $(001)$ , as shown in Fig. 2A, and B. Then a nanocrystal including  $i \times i$  chains (see Fig. 2C) can be represented as “ $iL_j$ ”, where  $j$  is the Degree of Polymerization (DP) of the chains, and the letter L can be A, B, and O, as demonstrated in Fig. 2A. For convenience, a nanocrystal including A (B, or O) facet is called Type-A (B, or O) crystal, for example, if the ends of  $6 \times 6$  chains comprise a  $(\bar{1}12)$  facet, and DP is 12 for each chain, it is assigned as 6A12, and it is a Type-A nanocrystal.

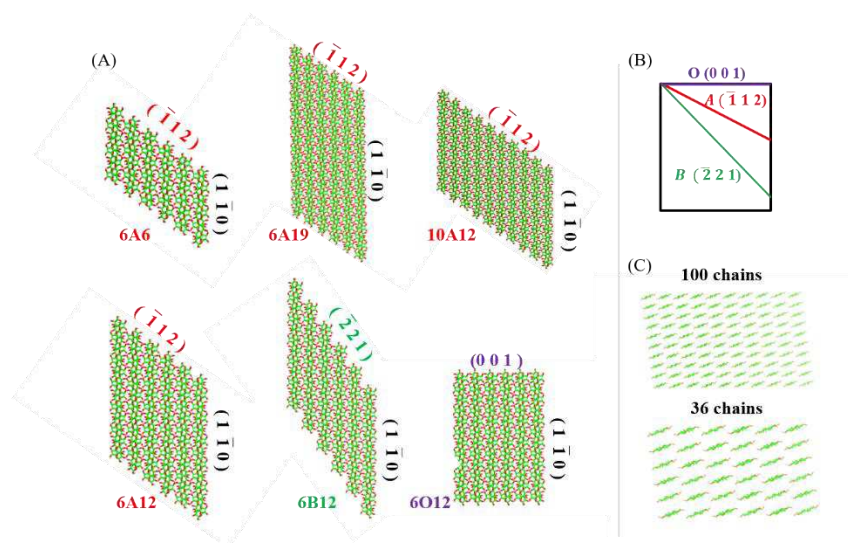


**Figure 2.** The structure and crystal facets of cellulose II nanocrystals. (A) The geometry of six types of cellulose II nanocrystal models. 6A6, 6A12, 6A19, and 10A12 denote  $6 \times 6 \times 6$ ,  $6 \times 6 \times 12$ ,  $6 \times 6 \times 19$ , and  $10 \times 10 \times 12$  the crystal models with the crystal facets  $(\bar{1}12)$ , respectively. 6B12 and 6O12 are  $6 \times 6 \times 12$

crystal models with  $(\bar{2} 2 1)$  and  $(0 0 1)$  as crystal facets respectively; (B) Three types of inclined crystal facets. (C)  $6 \times 6$  and  $10 \times 10$  are the chain numbers of the ab base plane projections.

### Hydroxymethyl conformations analysis

First, we focus on the influence of the cellulose II nanocrystal model on the hydroxymethyl group conformations. It is generally accepted that cellulose II has gt and gg conformations<sup>5-7</sup>, while the tg conformations are very rare<sup>10</sup>. The selected dihedral angle of the configuration is shown in Fig. 3A. There are three cases for the dihedral angle  $O_5-C_5-C_6-O_6$  on the anhydroglucose residue. One is that  $O_5$  and  $O_6$  are facing out of the chain, represented by  $\omega_1$ ; the second is that  $O_5$  and  $O_6$  are facing inward of the chain, represented by  $\omega_2$ ; all others are regarded as  $\omega_3$ .

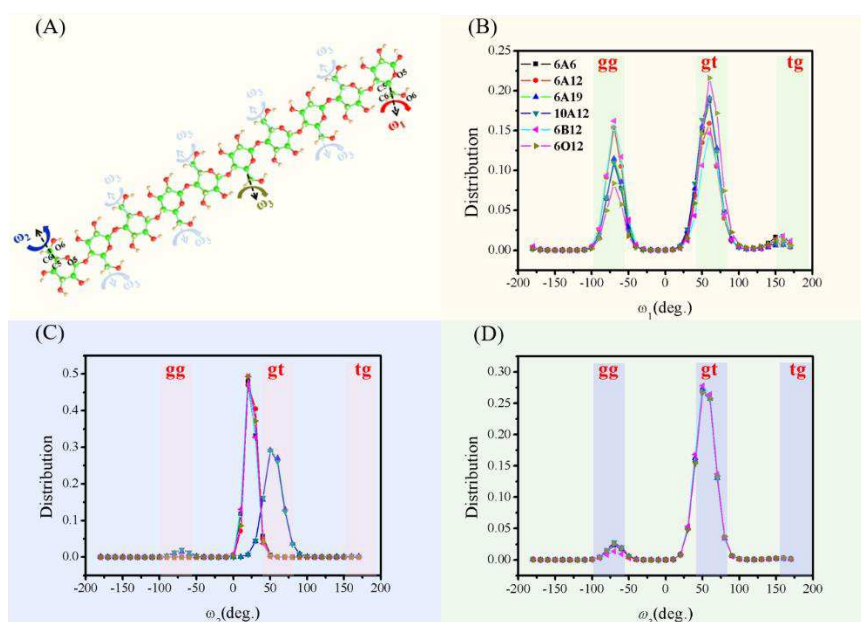


**Figure 3. The characteristic dihedral angle  $O_5-C_5-C_6-O_6$  distribution in the MD process.** (A) Definition of the torsion angle parameters of the hydroxymethyl group; (B), (C) and (D) are the dihedral angles  $\omega_1$ ,  $\omega_2$  and  $\omega_3$  distributions of the residues extracted from the MD trajectories in the last 1 ns, respectively.

Fig. 3B shows the distribution of the hydroxymethyl group conformations ( $\omega_1$ ) detected in the terminal residues. Obviously, two peaks appear near  $-60^\circ$  ( $\omega_1 \approx gg$ ) and  $60^\circ$  ( $\omega_1 \approx gt$ ), which means the hydroxymethyl groups frequently rotated between gt and gg position in 6A12, 6B12, and 6O12. In general, the gt distributions of 6O12, 6A12, and 6B12 are 21.60%, 15.89%, and 14.66%, respectively, indicating the more inclined the facet, the less gt conformation for hydroxymethyl group. Opposite results can be found in the gg distribution, where 6O12, 6A12, and 6B12 are 8.39%, 16.23%, and 15.40%, respectively, indicating that the gg distribution of the hydroxymethyl group decreases significantly with the incline of the nanocrystal facet. Therefore, compared to the flat crystal facet of 6O12, an inclined crystal facet can lead to fewer gt distribution and more gg distribution of hydroxymethyl group. Furthermore, the gt distribution of 6A6, 6A19, and 10A12 are 18.74%, 19.08%, and 19.08%, respectively, slightly larger than 6A12 (15.89%). The gg distribution

of 6A6, 6A19, and 10A12 are 11.16%, 11.51%, and 11.00%, respectively, which are somewhat smaller than 6A12. The current MD simulation still reproduces the minor conformations of the hydroxymethyl groups very well. For example, a minor peak also appears near tg ( $\omega_1 \approx 180^\circ$ ).

Fig. 3C shows the distribution of hydroxymethyl group conformations ( $\omega_2$ ) detected in the terminal residues of the crystal model. Compared with Fig. 3B, the hydroxymethyl group of  $\omega_2$  hardly rotates in gg position. What's more, there is almost no difference of hydroxymethyl conformation in 6A12, 6B12, and 6O12. Moreover, the distribution of hydroxymethyl groups is almost around  $20^\circ$  instead of  $60^\circ$  at the gt position. For Type-A models, as the chain and DP increase, the hydroxymethyl group of  $\omega_2$  gradually changes from about  $20^\circ$  to  $60^\circ$ , reaching the angular distribution range of the gt conformation. The distribution of hydroxymethyl group conformations ( $\omega_3$ ) detected in the internal anhydroglucose of the nanocrystal models is shown in Fig. 3D, where the hydroxymethyl group of  $\omega_3$  is almost at gt position with less at gg position. Compared with the conformations of  $\omega_2$  and  $\omega_3$  only at the gt position, the hydroxymethyl conformations of  $\omega_1$  are mainly distributed at the gg and gt positions, which can be inferred the possibility of different chemical properties at the chain end positions.

### Hydrogen bond analysis

The HB network can be regulated to obtain different nanocrystal facets; therefore, different properties of the reducing chain end can be obtained on different exposed facets, which may be necessary for subsequent chemical modification and specific potential applications. Hence, we are motivated to look for HBs differences in these nanocrystal models. Besides the usual HBs of cellulose, i.e., the  $O_2H \cdots O_6$  and  $O_6H \cdots O_6$ ,<sup>33,38</sup> more types of HBs were investigated. To obtain more detailed information about HBs in these models, the HBs strength is further calculated by optimizing the geometries in the highest HBs fraction. As represented in Supplementary Table S1, it manifests the average HBs analysis of the terminal residues in the six nanocrystal models. The average fraction  $\bar{F}$ , O-O distance and angle are averaged according to the HBs fraction (only the fraction large than 60% are considered). The fraction  $F$  of the  $j^{\text{th}}$  HB type in the  $i^{\text{th}}$  sample (there are eight HB types and 5000 sample in total) is defined as:

$$F_j^i = \frac{x_j^i}{\sum_j x_j^i} \quad (4)$$

The highest HBs fraction  $F_{\max}$  of the  $j^{\text{th}}$  HB type in the  $i^{\text{th}}$  sample is defined as:

$$F(j, \max) = \max\{F_j^i, i = 1, 5000\} \quad (5)$$

The average fraction  $\bar{F}$  of the  $j^{\text{th}}$  HB type in all samples is defined as:

$$\bar{F}_j = \frac{\sum_{i=1}^m (F_j^i \cdot N_i)}{\sum_{i=1}^m N_i} \quad (6)$$

Since  $N_i$  is basically the same, let  $N_i \approx n$ , then:

$$\bar{F}_j = \frac{\sum_{i=1}^m (F_j^i \cdot n)}{\sum_{i=1}^m n} = \frac{\sum_{i=1}^m (F_j^i \cdot n)}{m \cdot n} = \frac{\sum_{i=1}^m F_j^i}{m} \quad (7)$$

Hence  $\bar{F}$  in [Supplementary Table S1](#) is derived from Eq. (4), (6), and (7). In [Supplementary Table S1](#), the HBs are  $O_6H \cdots O_2$ ,  $O_2H \cdots O_2$ ,  $O_6H \cdots O_6$ ,  $O_3H \cdots O_6$ ,  $O_2H \cdots O_6$ ,  $O_6H \cdots O_3$ ,  $O_2H \cdots O_3$ , and  $O_3H \cdots O_5$ . It can be seen that  $O_6$  and  $O_2$  are most favorable in the HBs formation. We first consider the effects of different nanocrystal models 6A12, 6O12, and 6B12 on HBs. [Supplementary Fig. S1A](#) shows that 6O12 forms slightly more HBs than 6A12 and 6B12. Meanwhile, the  $\bar{F}$  of different HBs types in [Supplementary Fig. S1B](#) indicates that the HB fraction and type in 6A12 are maximum compared with 6O12 and 6B12. What's more, it seems less favorable for 6B12 to form HBs because it has only four types of HBs compared with 6A12 and 6O12. We speculate that the HB interaction between the adjacent terminal residues will first increase and then decreases with the increase of the inclined crystal plane. Therefore, it can be inferred that HBs are more likely to be formed in 6O12 and 6A12 than in 6B12.

According to [Supplementary Fig. S1C](#), the change of DP rarely affects the number of HBs in the Type-A nanocrystal models. More precisely, [Supplementary Fig. S1D](#) shows the types of HBs and the  $\bar{F}$  in different DP models, and it revealed that  $O_6H \cdots O_2$  has the most frequent appearance when DP increased from 6 to 19, followed by  $O_2H \cdots O_2$ ,  $O_2H \cdots O_6$ , and  $O_6H \cdots O_6$ . Alternatively,  $O_3H \cdots O_5$  seems to be a little impacted by the DP changes. In 6A6,  $O_3H \cdots O_4$  is gradually replaced by  $O_6H \cdots O_3$  as DP increases, indicating that the HBs involving  $O_4$  are not easy to form in Type-A nanocrystal models. Hence, the increase of DP in Type-A models will cause the change of HB type. As shown in [Supplementary Fig. S1E and F](#), the increasing chain from 6A12 to 10A12 brings a distinct HB number increase from 40 to 120 with the  $\bar{F}$  similar to each other. In addition,  $O_6H \cdots O_3$  is found in 6A12, and disappeared in 10A12.

Therefore, the HBs network changes with the interaction of terminal anhydroglucose between two adjacent chains on the exposed facet. In other words, the HB network can be formed by the adjacent anhydroglucose at the terminal chain changes with the inclined of the crystal facet. Hence, by regulating these HBs networks formed at the end of chains, different nanocrystal facets characteristics can be obtained. As shown in [Fig. 4](#), to obtain different types of HBs, the exposed facet composed of chain ends should be designed with an appropriate slope, which can be reflected in the terminal anhydroglucose position. For the convenience of description, we define terminal,

proximal, and distal position as the first, the second and remaining anhydroglucoses of a chain, respectively.

As shown in Fig. 4, the blue area represents the contact position between the neighbor anhydroglucose. It reveals that the types of HB for 6A12 and 6O12 is greater than that of 6B12. We speculate that it is related to the contact position of adjacent terminal anhydroglucoses. On the one hand, for the terminal and proximal position, it has the smaller anhydroglucose steric hindrance and the higher gt and/or gt distribution of the terminal hydroxymethyl group than in the distal position. Hence it is more likely to form types of HB at the terminal and/or the proximal position of 6A12 and 6O12 than at the distal position of 6B12. On the other hand, the contact area of 6A12 is slightly larger than that of 6O12, leading to more contact site of 6A12 to form more types of HB.

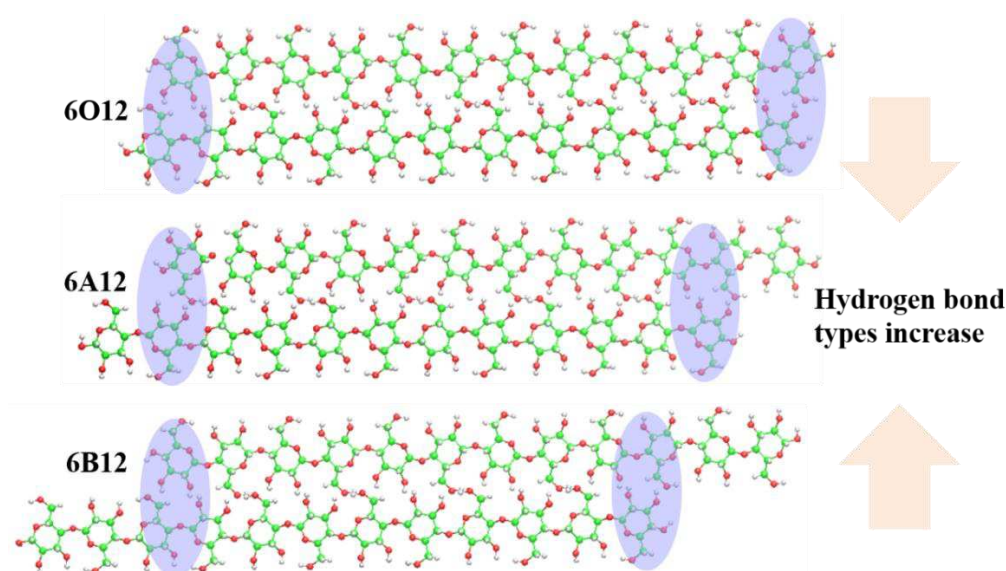


**Figure 4. The influence of inclined facet on the hydrogen bond formation.** Neighbor chain weak interaction of the terminal anhydroglucose varies in inclined crystal facets for cellulose II nanocrystal models.

The probability of HBs and nanocrystal models have no definite correlation, so we first identify the sample in which a certain type of HB gets the maximal probability for every model, then calculate the bond energy based on the electron charge density obtained by Eq. (1). Eight samples (the ONIOM models) are demonstrated in Supplementary Fig. S2A, where the HB with the maximal probability are marked; and the structural unit of each HBs are presented in Supplementary Fig. S 2B. Table 2 lists the detailed information of these HBs in nanocrystal models, the maximal probability is defined by  $F_{\max}$  based on Eq. (5). From the bond energy listed in Table 2, one can find that these HBs are weak to medium strength based on Emamian classification<sup>39</sup>. Most of the HBs' strengths are similar to each other. For example, the bond strength of  $O_2H \cdots O_6$  for 6A6 6A19 and 10A12 is about  $8.0 \text{ kcal}\cdot\text{mol}^{-1}$ , which is slightly greater than that of 6A12 and 6O12. The bond

energy of O<sub>2</sub>H···O<sub>2</sub> and O<sub>6</sub>H···O<sub>6</sub>, (corresponding to the weak to medium strength) increases from 6A6, 6A12, to 6A19, indicating the increase of nanocrystals DP can enhance the strength of the two HBs. Except for 6B12, the bond energy of O<sub>3</sub>H···O<sub>5</sub> is similar but slightly more extensive than that of 6A12 and 6O12. This is because its specific crystal facet that can make the related -O<sub>3</sub>H- end less affected by other HB. [Supplementary Table S2](#) shows the HBs type of these nanocrystal models, which is still highly consistent with the trend of HBs increasing from Type-O and Type-B to Type-A models.

**Table 2. Details of HBs in the sample where the fraction of an individual HB is highest among all samples for all the six models.** The HBs type, fraction ( $F_{\max}$ ) and O···O distance (Dist), HB angle (Ang), the electron density  $\rho(r)$  and corresponding HBs strength ( $E_{\text{HB}}$ ) are included.

Models	Type	$F_{\max}$	Dist/Å	Ang/°	$\rho(r)$	$E_{\text{HB}}/\text{kcal}\cdot\text{mol}^{-1}$
6A6	O <sub>2</sub> H···O <sub>2</sub>	0.925	2.748	162.870	0.035	-7.036
	O <sub>6</sub> H···O <sub>2</sub>	0.950	2.743	160.517	0.026	-4.969
	O <sub>6</sub> H···O <sub>6</sub>	0.923	2.767	162.871	0.036	-7.218
	O <sub>2</sub> H···O <sub>6</sub>	0.913	2.757	161.001	0.043	-8.901
	O <sub>3</sub> H···O <sub>5</sub>	0.938	2.738	160.252	0.025	-4.907
	O <sub>3</sub> H···O <sub>4</sub>	0.663	2.771	160.359	0.035	-7.161
6A12	O <sub>2</sub> H···O <sub>2</sub>	0.930	2.747	162.849	0.038	-7.732
	O <sub>6</sub> H···O <sub>2</sub>	0.956	2.749	161.395	0.033	-6.607
	O <sub>6</sub> H···O <sub>6</sub>	0.924	2.765	163.360	0.037	-7.517
	O <sub>2</sub> H···O <sub>6</sub>	0.891	2.754	159.548	0.023	-4.291
	O <sub>3</sub> H···O <sub>5</sub>	0.942	2.728	159.264	0.025	-4.725
	O <sub>6</sub> H···O <sub>3</sub>	0.671	2.767	162.158	0.038	-7.760
6A19	O <sub>2</sub> H···O <sub>2</sub>	0.960	2.762	164.572	0.039	-8.025
	O <sub>6</sub> H···O <sub>2</sub>	0.976	2.736	161.872	0.018	-3.306
	O <sub>6</sub> H···O <sub>6</sub>	0.923	2.761	162.411	0.038	-7.769
	O <sub>2</sub> H···O <sub>6</sub>	0.984	2.722	163.884	0.040	-8.064
	O <sub>3</sub> H···O <sub>5</sub>	0.974	2.707	160.031	0.024	-4.554
	O <sub>6</sub> H···O <sub>3</sub>	0.634	2.804	159.806	0.039	-8.034
10A12	O <sub>2</sub> H···O <sub>2</sub>	0.926	2.752	162.679	0.031	-6.131
	O <sub>6</sub> H···O <sub>2</sub>	0.962	2.746	161.647	0.037	-7.452
	O <sub>6</sub> H···O <sub>6</sub>	0.924	2.767	163.299	0.034	-6.918
	O <sub>2</sub> H···O <sub>6</sub>	0.914	2.752	160.441	0.040	-8.223
	O <sub>3</sub> H···O <sub>5</sub>	0.948	2.731	159.488	0.027	-5.237
6B12	O <sub>2</sub> H···O <sub>2</sub>	0.914	2.748	162.806	0.030	-6.029
	O <sub>6</sub> H···O <sub>2</sub>	0.921	2.750	160.769	0.023	-4.414
	O <sub>2</sub> H···O <sub>6</sub>	0.926	2.752	161.920	0.033	-6.646
	O <sub>3</sub> H···O <sub>5</sub>	0.930	2.732	159.522	0.042	-8.586
6O12	O <sub>6</sub> H···O <sub>2</sub>	0.844	2.756	161.307	0.035	-7.126
	O <sub>3</sub> H···O <sub>6</sub>	0.712	2.788	159.231	0.037	-7.412
	O <sub>2</sub> H···O <sub>6</sub>	0.764	2.786	158.271	0.020	-3.703
	O <sub>3</sub> H···O <sub>5</sub>	0.958	2.732	161.898	0.020	-3.751
	O <sub>6</sub> H···O <sub>3</sub>	0.872	2.747	161.186	0.026	-5.107

To quantify the stability of 6A12, 6B12, and 6O12, DFT calculations are conducted on their isolated chain of cellulose II. Generally, the lower the relative energy, the stable the structure. For an isolated chain of cellulose II nanocrystals, the relative energy is related to all possible facets in a model. Due to the antiparallel chain in cellulose II, when considering (1 1 0) facet, the corresponding (2 2 0) facet is also considered, as shown in [Supplementary Fig. S3](#), which includes two types of chain sequence: OCOCOC and COCOCO (as described above, O represents the Origin chain, C represents the Center chain); similarly, the crystal facets (0 1 0) and (0 2 0) are also considered together, including two types of chain sequence: OOOOOO and CCCCCC.

[Table 3](#) lists the DFT calculated energies of the three B3LYP-D3BJ DFT optimized 3×cello-tetramer chain sheet models in which Oxygen and Carbon atoms are fixed.  $\Delta E_{sheet}$  and  $\Delta E_{bind}$  is defined by Eq. (2) and (3). The BSSE counterpoise correction is estimated in vacuum to correlate the  $\Delta E_{sheet}$  and  $\Delta E_{bind}$  values between adjacent oligomers, which is used for further correlation of these two values in water circumstances.

**Table 3.** DFT energies of the B3LYP-D3BJ optimized 3×cello-tetramer chain sheet models (kcal·mol<sup>-1</sup> per residue).

models	DFT energies-vacuum			DFT energies-water		
	$\Delta E_{sheet}^a$	$\Delta E_{bind}$	BSSE	$\Delta E_{sheet}^a$	$\Delta E_{bind}$	
6A12	(1 1 0)+(2 2 0)	0.879	<b>-4.681</b>	1.228	0.454	-2.904
	(0 1 0)+(0 2 0)	2.435	<b>-2.979</b>	0.881	1.321	-2.010
6B12	(1 1 0) +(2 2 0)	2.872	<b>-3.480</b>	0.838	1.622	-1.902
	(0 1 0) +(0 2 0)	3.161	<b>-2.850</b>	0.698	1.845	-1.653
6O12	(1 1 0) +(2 2 0)	0.000	<b>-5.624</b>	1.401	0.000	-3.372
	(0 1 0) +(0 2 0)	1.477	<b>-4.023</b>	1.142	0.400	-3.138

<sup>a</sup> Relative to the plane of (1 1 0) by 6A12 model.

In vacuum, the three types of chain sheet models have different  $\Delta E_{bind}$  and, consequently, different  $\Delta E_{sheet}$ . These  $\Delta E_{bind}$  values for 6O12 structures are much lower than the rest residue. For example, for 6O12  $\Delta E_{bind}$  is -9.647 kcal·mol<sup>-1</sup> (the sum of (-5.624) + (-4.023)), lower than the value of 6.330 kcal·mol<sup>-1</sup> (the sum of (-3.480) + (-2.850)) for 6B12, and that of 7.660 kcal·mol<sup>-1</sup> the sum of for 6A12. The crystal facets (0 1 0) and (0 2 0) in the 6B12 model has the highest  $\Delta E_{sheet}$ , followed by the crystal facets (1 1 0) and (2 2 0) in 6B12 model, as well as the crystal facets (0 1 0) and (0 2 0) in 6A12 model. It can be concluded that 6O12 is the most stable nanocrystal model, corresponding to the fact that Type-O with the exposed facet (0 0 1) is the most common form of cellulose II nanocrystals.

In water, these structures become more stable, as demonstrated by the decrease of  $\Delta E_{sheet}$  from -0.4 (the minimal sheet energy gap between vacuum and water circumstance: 0.879 - 0.454) to -1.3 (the maximum sheet energy gap between vacuum and water circumstance: 3.161 - 1.845) kcal·mol<sup>-1</sup>

<sup>1</sup>, and  $\Delta E_{bind}$  from -0.9 (the minimal bind energy gap between vacuum and water circumstance: (2.979) – (-2.010)) to -2.3 (the maximum bind energy gap between vacuum and water circumstance: (-5.624) – (-3.372)) kcal·mol<sup>-1</sup> per residue compared to the values in vacuum. On the one hand, when the exposed facet is inclined, the adjacent chains are gradually separated from each other with the smaller contact area. Generally speaking, HB can play a role in stabilizing the structure. The structural stability from Type-O to Type-A and Type-B should have the same changing trend as the aforementioned HB quantity change, that is, first rise and then fall. However, the structural stability is not only affected by hydrogen bonds but also by other weak interactions, such as electrostatic interactions, van der Waals forces, and hydrophobic interactions, which are all related to the contact area of the neighbor chains. The larger the contact area, the weaker these interactions and the more unstable the structure. The continuously inclined facets from Type-O to Type-A and Type-B make the contact area of neighbor chains smaller, thereby weakening their weak interaction and leading to a more unstable three-dimensional structure. Therefore, the minimum energy of  $\Delta E_{sheet}$  and  $\Delta E_{bind}$  are still dominated by 6O12 in the different exposed cellulose II nanocrystals facets.

When considering the length (6A6, 6A12, 6A19) and number (6A12 and 10A12) of chains for Type-A crystal, we use the extended semi-empirical scheme GFN2-xTB. Fig. 5A shows the spacious distribution of chains in different models containing 2 or  $k^2$  ( $k=1, 2, 3, 4, 5,$  and  $6$ ) chains. Fig. 5B reveals that 6A6 is the most stable (with the lowest energy); the bigger the DP (the length of chain), the higher the energy, and hence the lower the stability. Furthermore, the increased rate of energy decreases with the increase of DP. Therefore, the structure will eventually stabilize, and more extension of DP will no longer affect its total energy. For the effect of the number of chains on the stability, one can find that 6A12 and 10A12 have almost equal energy (stability); so that the effect of the number of chains on stability can be ignored. Therefore, DP plays a significant impact on structural stability.

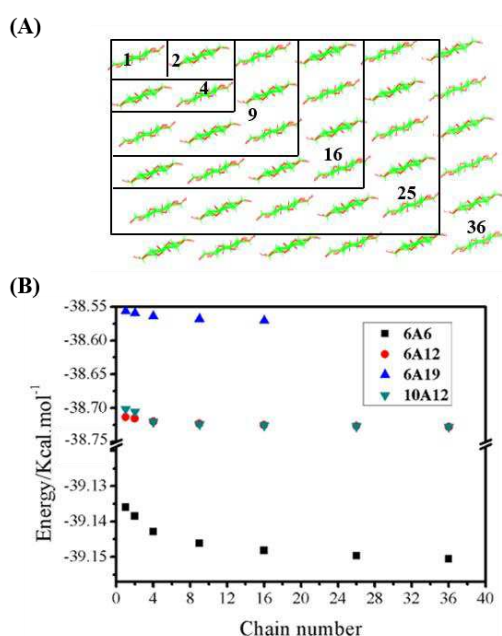


**Figure 5. Energy changes in the extension of the sheet chain.** (A) The crystal models of 1, 2, 4, 9, 16, 25, 36 chain numbers for 6A6, 6A12, 10A12 and 1, 2, 4, 9, 16 chain numbers for 6A19; (B) Energy comparison of Type-A models of different sizes.

## Conclusion

In summary, we have studied the properties of six cellulose II nanocrystal models via MD simulation and DFT calculations. The results revealed an obviously gt and gg position at  $\omega_1$  hydroxymethyl groups and mainly gt position at  $\omega_2$  and  $\omega_3$  hydroxymethyl groups. The HB types and quantities are further discussed. It turns out a slight superiority of the HB type for 6A12 compared with 6O12, and 6B12 has the least HB type, which can be attributed to the different contact sites of the anhydroglucose at the ends of adjacent chains. The HB strengths investigated by using the newly developed method are in the range of weak to medium, which provides an intuitive reference guide to further research on the content of HBs in organic polymers. A study on the relative structural stability indicated that the nanocrystal with a flat exposed facet is most stable, and the stability gradually decreases when the facets become more inclined. The chain length rather than the number of sidechains is more important for structural stability in Type-A nanocrystals. These results theoretically indicate that properties can be tuned by unambiguously designing the cellulose II nanocrystal facets. These findings will guide further research on syntheses novel celluloses with different physicochemical properties.

## Methods

All 6 models (6A12, 6B12, 6O12, 6A6, 6A19, and 10A12) are put into a periodic box to ensure a complete water box environment. A partial optimization of the TIP3P water configurations is minimized, followed by a full optimization of the whole system's solvated crystal model. The structures of the nanocrystal models are fixed constrained by a force of  $500 \text{ kcal}\cdot\text{mol}^{-1}$ . Then water configurations are equilibrated using the NVT ensemble with a gradual increase in temperature from 20 to 300 K in 300 ps, followed by the constant pressure dynamics simulations at 1 bar with isotropic position scaling and a pressure relaxation time of 2.0 ps throughout a MD simulation in 500 ps. Finally, an NPT simulation without any other constraint is implemented for 1 ns. All minimizations and dynamic simulations are performed with a dielectric constant of unity and a cut-off value for non-bonded pair interactions of  $10.0 \text{ \AA}$ . Throughout the equilibration NVT simulations, the positions of the solute crystal model's heavy atoms are constrained with a relatively weak force of  $10 \text{ kcal}\cdot\text{mol}^{-1}$ . Throughout the equilibration NVT simulations, the positions of the solute crystal model's heavy atoms are constrained with a relatively weak force of  $10 \text{ kcal}\cdot\text{mol}^{-1}$ . The SHAKE option<sup>40</sup> is adopted for bond interactions involving hydrogen atoms during dynamics calculations. All of the MD simulations are performed using the PMEMD module of the AMBER 12 package<sup>41</sup> combined with the Glycam06<sup>42</sup> carbohydrate parameter set. The MD trajectories are analyzed by the PTRAJ module of the AMBER 12 package and visualized using Visual Molecular Dynamics (VMD) 1.9.1 software.<sup>43</sup>

In the weak interaction theory, a variety of methods can be used to analyze the HBs interaction.<sup>39,44</sup> Recently, a new method has shown that the bonding critical point (BCP) has a linear relationship with HB strength.<sup>45</sup> It defines the calculation of the HB energy ( $\text{kcal}\cdot\text{mol}^{-1}$ ) as follows,

$$y = -223.08 \times \rho_{BCP}(a.u.) + 0.7423 \quad (1)$$

where  $\rho$  is the electron charge density at the BCPs of HB. Based on Bader's theory, topological analyses of the electron charge density  $\rho$  at the BCPs is performed using atoms-in molecules (AIM) analysis<sup>46</sup> in Multiwfn program<sup>47,48</sup>, and then it is visualized by the VMD program. To obtain accurate HBs geometry, the ONIOM model<sup>49</sup> is used to further optimize HB's geometry after the MD simulation. The wB97XD functional, together with the def2-SVP<sup>50</sup> basis set, is used as a high layer to optimize the involving HBs parts (two anhydroglucose involving HB are selected), and the UFF force field<sup>51</sup> is used as a lower layer to describe the remaining parts. Then the optimized HB structure by ONIOM model is further studied by the AIM analysis to obtain the electron charge density  $\rho$  for the calculation of HB strength.

The isolated chain sheet models are initially optimized using the AMBER/Glycam06 parameters, followed by the DFT optimization with 3×cello-tetramer chain sheet models for 6A12, 6B12 and 6O12. The reason that three cello-tetramer is considered is that the three-chain sheet models can well depict the interaction with the adjacent chain, the double of the three chains can form the crystal plane, which is reasonable to adopt a 3×cello-tetramer chain in DFT calculation. Only the hydrogen atoms' position with the added terminal methyl groups are optimized in Gaussian09<sup>52</sup>, while all other atoms are fixed in position. In the DFT optimization, the present study used B3LYP-D3BJ function is coupled with the 6-31g(d) basis set. The single-point energy of the optimized model is then calculated using the 6-31+g(d,p) basis set. Besides, the solvent effects are mimicked by using the Solvation Model Based on Density (SMD)<sup>53</sup> in water. The binding energy ( $\Delta E_{bind}$ ) between adjacent oligomers is calculated as the difference between the DFT energies of the total model  $E_{total}$  and its separate parts ( $E_1$  and  $E_2$ ), as defined by the following equations (Eq).

$$\Delta E_{bind} = E_{total} - E_i \quad (2)$$

$$\Delta E_{sheet} = E_i + \Delta E_{bind} \quad (3)$$

where  $i=1, 2$ .  $E_1$  and  $E_2$  represent the energy of the two different oligomers, respectively. The three-chain sheet models  $E_2$  represent the interior oligomer's energy and the remainder of the sheet, respectively. The stabilization energy of the chain sheet ( $\Delta E_{sheet}$ ) is defined as the sum of  $E_i$  and  $\Delta E_{bind}$ , which implies the total energy of the oligomer  $i$  with the contribution of neighbor chain interaction. The basis set superposition error (BSSE) is estimated using the counterpoise method.<sup>52,54</sup>

GFN-xTB is one of the most newly developed semi-empirical DFT methods developed by the Grimme team<sup>55-57</sup>. It is an eXtended Tight-Binding semi-empirical program package (xtb) specially designed to calculate reasonable geometry, vibration frequency, and noncovalent interaction (GFN). Here we adopt it for the fast computation of 6A6, 6A12, 6A19, and 10A12, respectively. The geometry minimized by Amber is used to further optimization by GFN2-xTB with the C and O atoms fixed underwater circumstances.

## References

- 1 O'Sullivan, A. C. Cellulose: the structure slowly unravels. *Cellulose* **4**, 173-207, (1997).
- 2 Chtchigrovsky, M. *et al.* Functionalized Chitosan as a Green, Recyclable, Biopolymer-Supported Catalyst for the [3+2] Huisgen Cycloaddition. *Angew. Chem. Int. Ed.* **48**, 5916-5920, (2009).
- 3 Lucia, L. & Rojas, O. *The Nanoscience and Technology of Renewable Biomaterials*. (ed. Lucian, A. and Lucia, Orlando, J. Rojas) (Blackwell, 2009).
- 4 Oksman, K., Mathew, A. P., Bismarck, A., Rojas, O. & Sain, M. In Cellulose Nanocomposites: Processing, Characterization and Properties. *J. Biobased Mater. Bio.* 53-68 (2006).
- 5 Langan, P., Nishiyama, Y. & Chanzy, H. A Revised Structure and Hydrogen-Bonding System in Cellulose II from a Neutron Fiber Diffraction Analysis. *J. Am. Chem. Soc.* **121** (1999).
- 6 Langan, P., Nishiyama, Y. & Chanzy, H. X-ray structure of mercerized cellulose II at 1 Å resolution. *Biomacromolecules* **2**, 410-416, (2001).
- 7 Langan, P., Sukumar, N., Nishiyama, Y. & Chanzy, H. Synchrotron X-ray structures of cellulose I $\beta$  and regenerated cellulose II at ambient temperature and 100 K. *Cellulose* **12**, 551-562, (2005).
- 8 Tetsuo *et al.* "Nematic Ordered Cellulose": A Concept of Glucan Chain Association. *Biomacromolecules* **2**, 1324-1330, (2001).
- 9 Kennedy, J. F. & Hossain, A. Cellulose and wood: Chemistry and technology. *Carbohydr. Polym.* **14**, 337-338, (1991).
- 10 Nishiyama, Y., Sugiyama, J., Chanzy, H. & Langan, P. Crystal structure and hydrogen bonding system in cellulose I( $\alpha$ ) from synchrotron X-ray and neutron fiber diffraction. *J. Am. Chem. Soc.* **125**, 14300-14306, (2003).
- 11 Nishiyama, Y., Langan, P. & Chanzy, H. Crystal Structure and Hydrogen-Bonding System in Cellulose I $\beta$  from Synchrotron X-ray and Neutron Fiber Diffraction. *J. Am. Chem. Soc.* **124**, 9074-9082, (2002).
- 12 French, A. D. Chapter 2-Combining Computational Chemistry and Crystallography for a Better Understanding of the Structure of Cellulose. *Elsevier* **67**, 19-93, (2012).
- 13 Navarrete-López, A. M., San-Román, M. L. & Zicovich-Wilson, C. M. The influence of the DFT approach on the structure and relative stability of models for cellulose I allomorphs. *Theor. Chem. Acc.* **135**, 136, (2016).
- 14 Goldberg, R. N. *et al.* A thermodynamic investigation of the cellulose allomorphs: Cellulose(am), cellulose I $\beta$ (cr), cellulose II(cr), and cellulose III(cr). *J. Chem. Thermodyn.* **81**, 184-226, (2015).
- 15 Yang, H. & Kubicki, J. D. A density functional theory study on the shape of the primary cellulose microfibril in plants: effects of C6 exocyclic group conformation and H-bonding. *Cellulose* **27**, 2389-2402, (2020).

- 16 Srivastava, D., Kuklin, M. S., Ahopelto, J. & Karttunen, A. J. Electronic band structures of pristine and chemically modified cellulose allomorphs. *Carbohydr. Polym.* **243**, 116440, (2020).
- 17 Nishiyama, Y. Molecular interactions in nanocellulose assembly. *Philos Trans A Math Phys. Eng. Sci.* **376**, 20170047, (2018).
- 18 Rocha, I. M., Galvão, T. L. P., Sapei, E., Ribeiro da Silva, M. D. M. C. & Ribeiro da Silva, M. A. V. Levoglucosan: A Calorimetric, Thermodynamic, Spectroscopic, and Computational Investigation. *J. Chem. Eng. Data* **58**, (2013).
- 19 Yui, T. & Hayashi, S. Structural stability of the solvated cellulose III crystal models: a molecular dynamics study. *Cellulose* **16**, 151-165, (2009).
- 20 Uto, T., Mawatari, S. & Yui, T. Theoretical study of the structural stability of molecular chain sheet models of cellulose crystal allomorphs. *J. Phys. Chem. B* **118**, 9313-9321, (2014).
- 21 Kubicki, J. D. *et al.* The Shape of Native Plant Cellulose Microfibrils. *Sci. Rep.* **8**, 13983, (2018).
- 22 Hohenberg, P. & Kohn, W. Inhomogeneous Electron Gas. *Phys. Rev.* **136**, B864-B871, (1964).
- 23 Kohn, W. & Sham, L. J. Self-Consistent Equations Including Exchange and Correlation Effects. *Phys. Rev.* **140**, A1133-A1138, (1965).
- 24 Neese, F. Software update: the ORCA program system, version 4.0. *WIREs Computational Molecular Science* **8**, e1327, (2018).
- 25 Christoph *et al.* GFN2-xTB-An Accurate and Broadly Parametrized Self-Consistent Tight-Binding Quantum Chemical Method with Multipole Electrostatics and Density-Dependent Dispersion Contributions. *J. Chem. Theory Comput.* **15**, 1652-1671, (2019).
- 26 Řezáč, J. & Hobza, P. Advanced Corrections of Hydrogen Bonding and Dispersion for Semiempirical Quantum Mechanical Methods. *J. Chem. Theory Comput.* **8**, 141-151, (2012).
- 27 Rabideau, B. D. & Ismail, A. E. Mechanisms of hydrogen bond formation between ionic liquids and cellulose and the influence of water content. *Phys. Chem. Chem. Phys.* **17**, 5767-5775, (2015).
- 28 Zhang, J. *et al.* NMR spectroscopic studies of cellobiose solvation in EmimAc aimed to understand the dissolution mechanism of cellulose in ionic liquids. *Phys. Chem. Chem. Phys.* **12**, 1941-1947, (2010).
- 29 Guo, Y. & Wu, P. Investigation of the hydrogen-bond structure of cellulose diacetate by two-dimensional infrared correlation spectroscopy. *Carbohydr. Polym.* **74**, 509-513, (2008).
- 30 Sasaki, M., Adschiri, T. & Arai, K. Production of cellulose II from native cellulose by near- and supercritical water solubilization. *J. Agric. Food. Chem.* **51**, 5376-5381, (2003).
- 31 Glasser, W. G. *et al.* About the structure of cellulose: debating the Lindman hypothesis. *Cellulose* **19**, 589-598, (2012).
- 32 Nishiyama, Y., Langan, P., Wada, M. & Forsyth, V. T. Looking at hydrogen bonds in cellulose. *Acta Crystallogr. D Biol. Crystallogr.* **66**, 1172-1177, (2010).
- 33 Hayakawa, D., Nishiyama, Y., Mazeau, K. & Ueda, K. Evaluation of hydrogen bond networks in cellulose I $\beta$  and II crystals using density functional theory and Car-Parrinello molecular dynamics. *Carbohydr. Res.* **449**, 103-113, (2017).
- 34 Idström, A. *et al.* <sup>13</sup>C NMR assignments of regenerated cellulose from solid-state 2D NMR spectroscopy. *Carbohydr. Polym.* **151**, 480-487, (2016).
- 35 Nishiyama, Y., Johnson, G. P., French, A. D., Forsyth, V. T. & Langan, P. J. B. Neutron crystallography, molecular dynamics, and quantum mechanics studies of the nature of hydrogen bonding in cellulose I $\beta$ . *Biomacromolecules* **9**, 3133-3140 (2008).

- 36 Gonzalez-Outeiriño, J., Kirschner, K. N., Thobhani, S. & Woods, R. J. Reconciling solvent effects on rotamer populations in carbohydrates: A joint MD and NMR analysis. *Can. J. Chem.* **84**, 569-579, (2006).
- 37 Gomes, T. C. & Skaf, M. S. Cellulose-builder: a toolkit for building crystalline structures of cellulose. *J. Comput. Chem.* **33**, 1338-1346, (2012).
- 38 Yui, T., Nishimura, S., Akiba, S. & Hayashi, S. Swelling behavior of the cellulose I $\beta$  crystal models by molecular dynamics. *Carbohydr. Res.* **341**, 2521-2530, (2006).
- 39 Araujo, C. *et al.* Hydrogen Bond Dynamics of Cellulose through Inelastic Neutron Scattering Spectroscopy. *Biomacromolecules* **19**, 1305-1313, (2018).
- 40 Ryckaert, J.-P., Ciccotti, G. & Berendsen, H. J. C. Numerical integration of the cartesian equations of motion of a system with constraints: molecular dynamics of n-alkanes. *J. Comput. Phys.* **23**, 327-341, (1977).
- 41 Case, D. *et al.* AMBER 12, University of California, San Francisco. (2012).
- 42 Kirschner, K. N. *et al.* GLYCAM06: A generalizable biomolecular force field. *Carbohydrates. J. Comput. Chem.* **29**, 622-655, (2008).
- 43 Humphrey, W., Dalke, A. & Schulten, K. VMD: visual molecular dynamics. *J. Mol. Graph.* **14**, 33-38, 2 (1996).
- 44 Řezáč, J. & Hobza, P. Benchmark Calculations of Interaction Energies in Noncovalent Complexes and Their Applications. *Chem. Rev.* **116**, 5038-5071, (2016).
- 45 Emamian, S., Lu, T., Kruse, H. & Emamian, H. Exploring Nature and Predicting Strength of Hydrogen Bonds: A Correlation Analysis Between Atoms-in-Molecules Descriptors, Binding Energies, and Energy Components of Symmetry-Adapted Perturbation Theory. *J. Comput. Chem.* **40**, 2868-2881, (2019).
- 46 Orville-Thomas, W. J. *Atoms in Molecules - a Quantum Theory*: Richard F.W. Bader, Clarendon Press, Oxford, U.K. *J. Mol. Struct.* **360**, 175, (1996).
- 47 Lu, T. & Chen, F. Quantitative analysis of molecular surface based on improved Marching Tetrahedra algorithm. *J. Mol. Graph. Model* **38**, 314-323, (2012).
- 48 Lu, T. & Chen, F. Multiwfn: a multifunctional wavefunction analyzer. *J. Comput. Chem.* **33**, 580-592, (2012).
- 49 Dapprich, S., Komáromi, I., Byun, K. S., Morokuma, K. & Frisch, M. J. A new ONIOM implementation in Gaussian98. Part I. The calculation of energies, gradients, vibrational frequencies and electric field derivatives. *J. Mol. Struct-Theochem.* **461-462**, 1-21, (1999).
- 50 Yanai, T., Tew, D. P. & Handy, N. C. A new hybrid exchange–correlation functional using the Coulomb-attenuating method (CAM-B3LYP). *Chem. Phys. Lett.* **393**, 51-57, (2004).
- 51 Rappe, A. K., Casewit, C. J., Colwell, K. S., Goddard, W. A. & Skiff, W. M. UFF, a full periodic table force field for molecular mechanics and molecular dynamics simulations. *J. Am. Chem. Soc.* **114**, 10024-10035, (1992).
- 52 Frisch, M. *et al.* Gaussian 09 (Revision D.01). Gaussian, Inc., Wallingford, CT (2009).
- 53 Marenich, A. V., Cramer, C. J. & Truhlar, D. G. Universal solvation model based on solute electron density and on a continuum model of the solvent defined by the bulk dielectric constant and atomic surface tensions. *J. Phys. Chem. B* **113**, 6378-6396, (2009).
- 54 Boys, S. F. & Bernardi, F. The calculation of small molecular interactions by the differences of separate total energies. Some procedures with reduced errors. *Mol. Phys.* **19**, 553-566, (1970).
- 55 Grimme, S., Bannwarth, C. & Shushkov, P. A Robust and Accurate Tight-Binding Quantum Chemical Method for Structures, Vibrational Frequencies, and Noncovalent Interactions of

- Large Molecular Systems Parametrized for All spd-Block Elements ( $Z = 1-86$ ). *J. Chem. Theo. Comput.* **13**, 1989-2009, (2017).
- 56 Philipp, P., Eike, C., Sebastian, E. & Stefan, G. A Robust Non-Self-Consistent Tight-Binding Quantum Chemistry Method for large Molecules. *ChemRxiv*, **1**, 1-19, (2019).
- 57 Bannwarth, C., Ehlert, S. & Grimme, S. GFN2-xTB—An Accurate and Broadly Parametrized Self-Consistent Tight-Binding Quantum Chemical Method with Multipole Electrostatics and Density-Dependent Dispersion Contributions. *J. Chem. Theo. Comput.* **15**, 1652-1671, (2019).

## Acknowledgments

This work is partially supported by the National Key Research and Development Program of China (Grant No. 2017YFB0202104, 2018YFB0204301).

## Author Contributions

Z.T., Y.S. and K.Q.L. proposed the research direction, designed the computations and guided the project. C.L. and K.L.L. performed the computations. H.H. and J.F.L. perform the analysis with constructive discussions. C.L., J.L. and W.-Q.H. analyzed the results and drafted the manuscript. All authors discussed the results and revised the manuscript.

## Additional Information

### Supplementary information

**Competing Interests:** The authors declare no competing interests.

# Figures

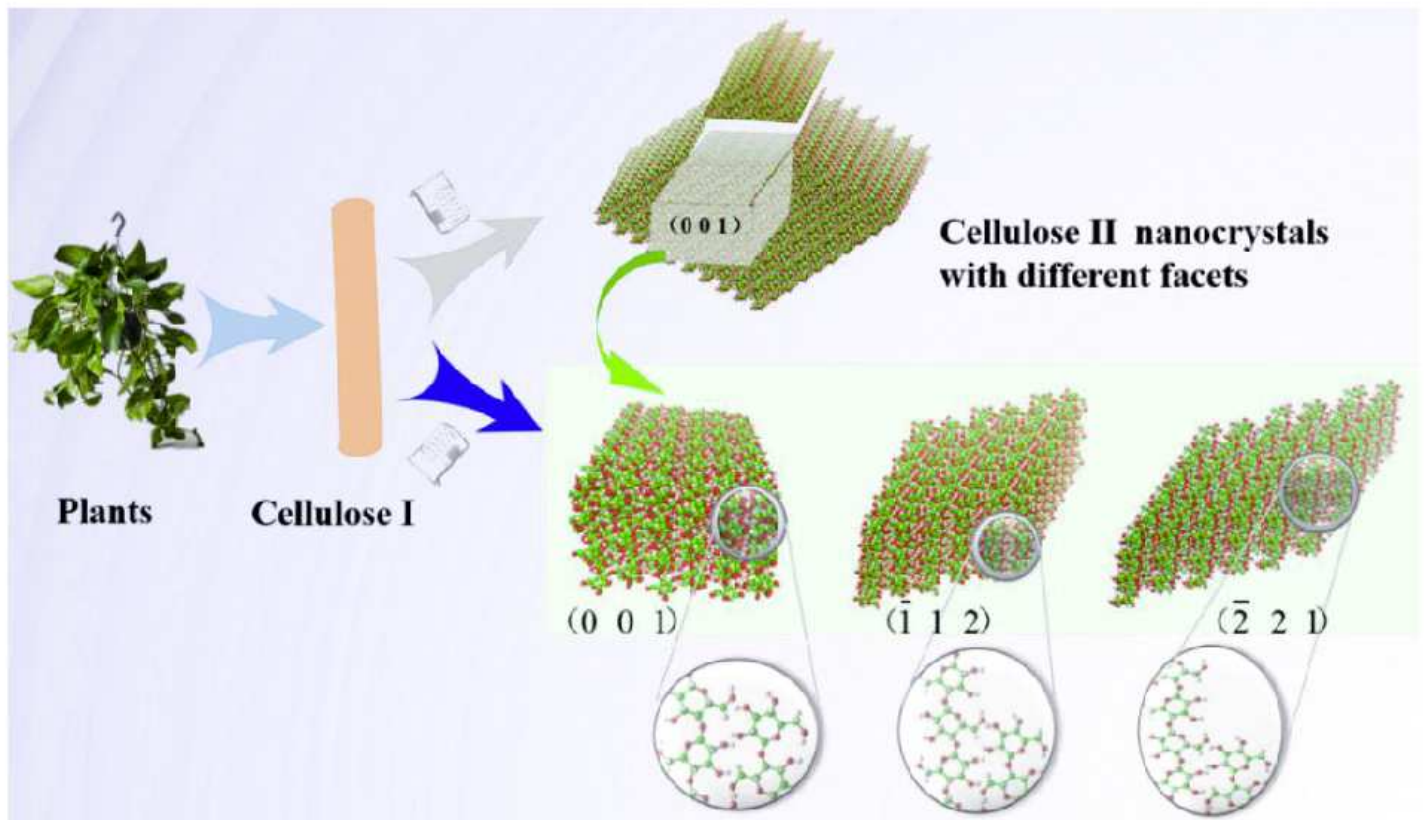


**Figure 1**

Cellulose II nanocrystals with different exposed facets. Cellulose I represent the native material in plants, from which Cellulose II can be synthesized. The facet  $(0\ 0\ 1)$  is the primary crystal facets of cellulose II nanocrystals,  $(\bar{1}\ 1\ 2)$  and  $(\bar{2}\ 2\ 1)$  are the inclined facets of cellulose II.

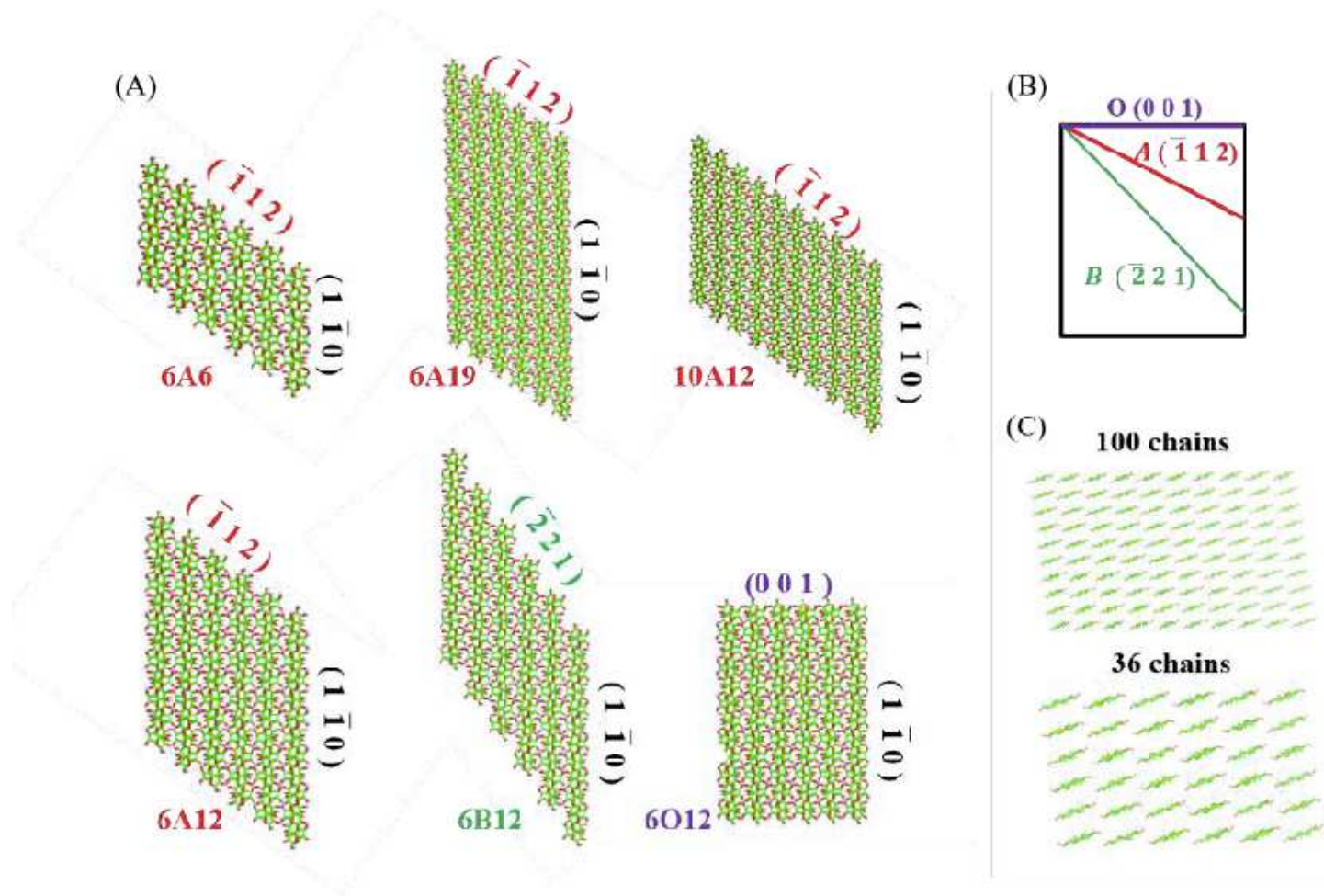


**Figure 2**

The structure and crystal facets of cellulose II nanocrystals. (A) The geometry of six types of cellulose II nanocrystal models. 6A6, 6A12, 6A19, and 10A12 denote 6×6×6, 6×6×12, 6×6×19, and 10×10×12 the crystal models with the crystal facets  $(1\ 1\ 2)$ , respectively. 6B12 and 6O12 are 6×6×12 crystal models with  $(2\ 2\ 1)$  and  $(0\ 0\ 1)$  as crystal facets respectively; (B) Three types of inclined crystal facets. (C) 6×6 and 10×10 are the chain numbers of the ab base plane projections.

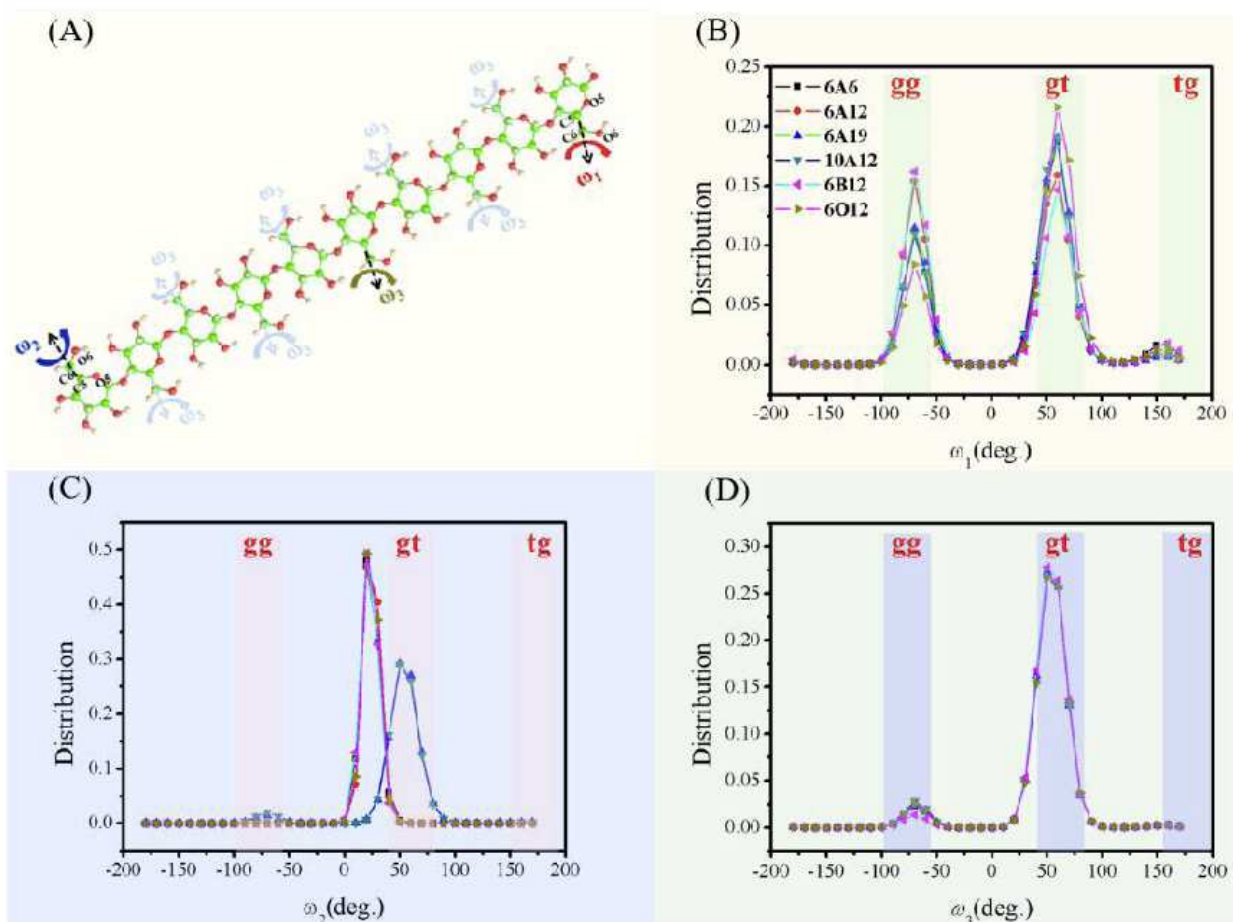


**Figure 3**

The characteristic dihedral angle O5-C5-C6-O6 distribution in the MD process. (A) Definition of the torsion angle parameters of the hydroxymethyl group; (B), (C) and (D) are the dihedral angles  $\omega_1$ ,  $\omega_2$  and  $\omega_3$  distributions of the residues extracted from the MD trajectories in the last 1 ns, respectively.

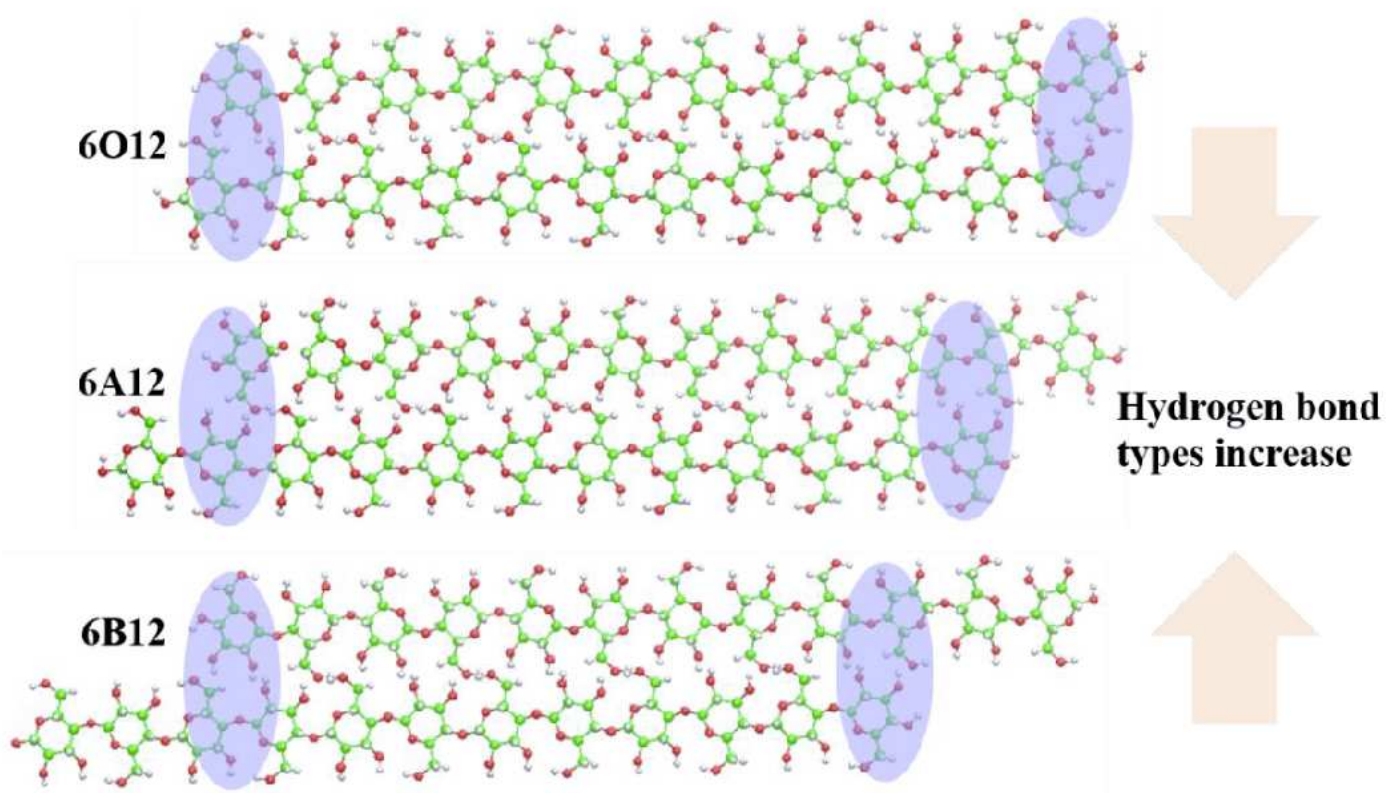
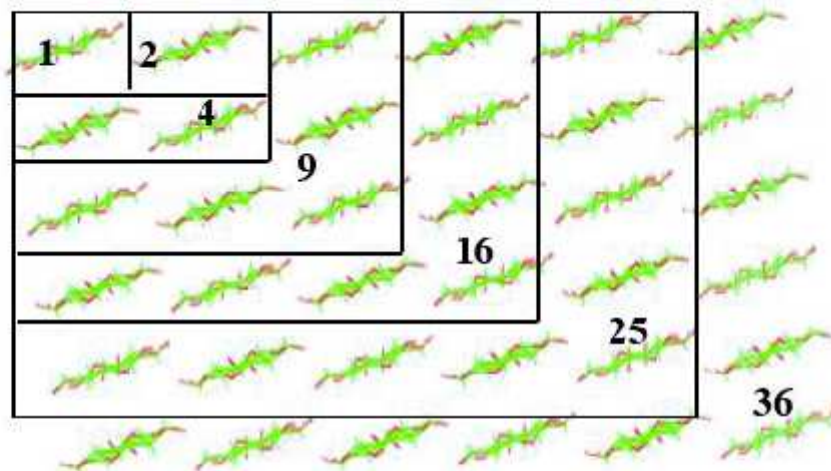


**Figure 4**

The influence of inclined facet on the hydrogen bond formation. Neighbor chain weak interaction of the terminal anhydroglucose varies in inclined crystal facets for cellulose II nanocrystal models.

(A)



(B)

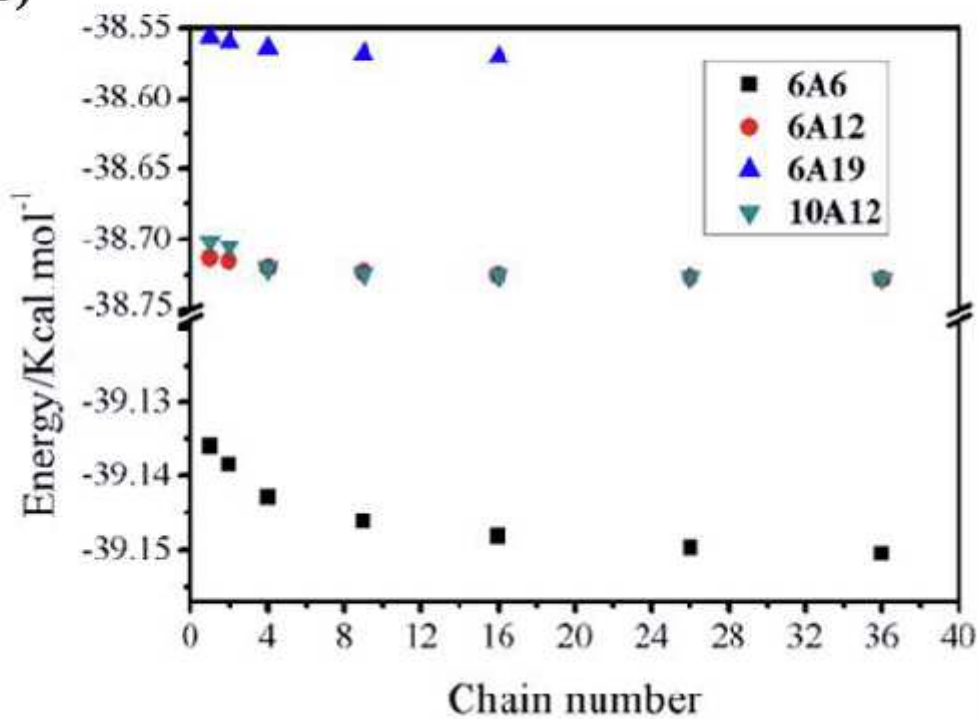


Figure 5

Energy changes in the extension of the sheet chain. (A) The crystal models of 1, 2, 4, 9, 16, 25, 36 chain numbers for 6A6, 6A12, 10A12 and 1, 2, 4, 9, 16 chain numbers for 6A19; (B) Energy comparison of Type-A models of different sizes.

## Supplementary Files

This is a list of supplementary files associated with this preprint. Click to download.

- [0209SupplementaryInformationv2.pdf](#)